

Observing one-divalent-metal-ion-dependent and histidine-promoted His-Me family I-Ppol nuclease catalysis *in crystallo*

Caleb Chang, Grace Zhou, Yang Gao*

Department of Biosciences, Rice University, Houston, United States

Abstract Metal-ion-dependent nucleases play crucial roles in cellular defense and biotechnological applications. Time-resolved crystallography has resolved catalytic details of metal-ion-dependent DNA hydrolysis and synthesis, uncovering the essential roles of multiple metal ions during catalysis. The histidine-metal (His-Me) superfamily nucleases are renowned for binding one divalent metal ion and requiring a conserved histidine to promote catalysis. Many His-Me family nucleases, including homing endonucleases and Cas9 nuclease, have been adapted for biotechnological and biomedical applications. However, it remains unclear how the single metal ion in His-Me nucleases, together with the histidine, promotes water deprotonation, nucleophilic attack, and phosphodiester bond breakage. By observing DNA hydrolysis *in crystallo* with His-Me I-Ppol nuclease as a model system, we proved that only one divalent metal ion is required during its catalysis. Moreover, we uncovered several possible deprotonation pathways for the nucleophilic water. Interestingly, binding of the single metal ion and water deprotonation are concerted during catalysis. Our results reveal catalytic details of His-Me nucleases, which is distinct from multi-metal-ion-dependent DNA polymerases and nucleases.

*For correspondence: yg60@rice.edu

Competing interest: The authors declare that no competing interests exist.

Funding: See page 13

Preprint posted

30 May 2024

Sent for Review

30 May 2024

Reviewed preprint posted

01 July 2024

Reviewed preprint revised

31 July 2024

Version of Record published

14 August 2024

Reviewing Editor: Axel T Brunger, Stanford University School of Medicine, Howard Hughes Medical Institute, United States

© Copyright Chang et al. This article is distributed under the terms of the [Creative Commons Attribution License](#), which permits unrestricted use and redistribution provided that the original author and source are credited.

eLife assessment

Chang et al. have investigated the catalytic mechanism of I-Ppol nuclease, a one-metal-ion dependent nuclease, by time-resolved X-ray crystallography using soaking of crystals with metal ions under different pH conditions. This **convincing** study revealed that I-Ppol catalyzes the reaction process through a single divalent cation. The study uncovers **important** details of the roles of the metal ion and the active site histidine in catalysis.

Introduction

Mg²⁺-dependent nucleases play fundamental roles in DNA replication and repair (Kao and Bambara, 2003; Shen et al., 2005; Marti and Fleck, 2004; Mimitou and Symington, 2009), RNA processing (Patel and Steitz, 2003; Abelson et al., 1998; Chu and Rana, 2007; Moore and Proudfoot, 2009), as well as immune response and defense (James et al., 1996; Sorek et al., 2008; Tock and Dryden, 2005). Moreover, they are widely employed for genome editing in biotechnological and biomedical applications (Adli, 2018; Carroll, 2014). These nucleases are proposed to cleave DNA through a SN₂-type reaction, in which a water molecule, or sometimes, a tyrosine side chain (Grindley et al., 2006), initiates the nucleophilic attack on the scissile phosphate with the help of metal ions (Yang, 2011). Metal ions can orient and stabilize the binding of the negatively charged nucleic acid backbone (Chen et al., 2017), promoting proton transfer, nucleophilic attack, and stabilization of the transition

state. As a highly varied family of enzymes, Mg^{2+} -dependent nucleases can be broadly categorized by the number of metal ions captured in their active site. So far, Mg^{2+} -dependent nucleases with one and two metal ions have been observed. In the two- Mg^{2+} -ion-dependent nuclease, a metal ion binds on the leaving group side of the scissile phosphate (Me^{2+}_b) while the other binds on the nucleophile side (Me^{2+}_a). In one-metal-ion-dependent nucleases, only the metal ion corresponding to the B site in two-metal-ion-dependent nucleases is present (Yang, 2008). Moreover, transiently bound metal ions have been identified in the previously thought two-metal-ion RNaseH (Samara and Yang, 2018) and EndoV nucleases (Wu et al., 2019) via time-resolved X-ray crystallography, proposed to play key roles in various stages of their catalysis. Similarly, catalysis in the one-metal-ion-dependent APE1 nuclease has been observed *in crystallo*, but mechanistic details regarding its metal-ion dependence have not been thoroughly explored (Freudenthal et al., 2015; Whitaker et al., 2018; Dupureur, 2010). There also exist three- Zn^{2+} -dependent nucleases, with two Zn^{2+} binding in the A- and B-equivalent positions, while the third Zn^{2+} coordinating the sp oxygen on the nucleophile side of the scissile phosphate (Garcin et al., 2008). However, it remains unclear how the single metal ion in one-metal-ion-dependent nucleases is capable of aligning the substrate, promoting deprotonation and nucleophilic attack, and stabilizing the pentacovalent transition state.

A large subfamily of one-metal-ion-dependent nucleases consist of histidine-metal (His-Me) nucleases that perform critical tasks in biological pathways such as apoptosis (Arnoult et al., 2003; Lin et al., 2016), extracellular defense (Cheng et al., 2002; Hsia et al., 2004), intracellular immunity (CRISPR–Cas9) (Doudna and Charpentier, 2014; Ran et al., 2013), and intron homing (homing endonuclease) (Chevalier and Stoddard, 2001; Stoddard, 2005). Despite sharing poor sequence homology, the structural cores and active sites of His-Me nucleases are highly conserved and thus are proposed to catalyze DNA hydrolysis through a similar mechanism (Yang, 2011; Stoddard, 2005; Wu et al., 2020). Surrounded by two beta sheets and an alpha helix, the His-Me nucleases active sites all contain a single metal ion, a histidine, and an asparagine (Figure 1A, Figure 1—figure supplement 1A, and Figure 1—figure supplement 2). The asparagine residue helps to stabilize metal ion binding whereas the strictly conserved histidine is suggested to deprotonate a nearby water for nucleophilic attack toward the scissile phosphate (Galburt et al., 1999; Pommer et al., 2001; Li et al., 2003; Shen et al., 2004). To this day, the dynamic reaction process of DNA hydrolysis by His-Me nucleases has never been visualized, and the mechanism of single metal-ion-dependent and histidine-promoted catalysis remains unclear. Emerging genome editing and disease treatment involving CRISPR–Cas9 emphasize the importance of understanding the catalytic mechanism of DNA hydrolysis by His-Me nucleases (Schwank et al., 2013; Sharma et al., 2021; Khan et al., 2016). Recent crystal and cryo-electron microscope structures of Cas9 have captured the His-Me family Cas9 histidine–asparagine–histidine (HNH) active site engaged with DNA before and after cleavage (Sun et al., 2019; Zhang et al., 2020; Zhu et al., 2019; Das et al., 2023). However, due to the relatively low resolution and the static nature of the structures, key catalytic details, such as metal ion dependence, transition-state stabilization, and alternative deprotonation pathways, remain elusive. Moreover, the large size and multiple conformational checkpoints during Cas9 catalysis (Sun et al., 2019; Zhang et al., 2020; Zhu et al., 2019; Das et al., 2023) hinder *in crystallo* observation of Cas9 catalysis.

I-Ppol is a well-characterized intron-encoded homing endonuclease member of the *physarum polycephalum* slimemold. By 1999, Stoddard and colleagues were able to capture intermediate structures of I-Ppol complexed with DNA before and after product formation (Galburt et al., 1999; Flick et al., 1998). We herein employed I-Ppol as a model system and applied time-resolved crystallography to observe the catalytic process of His-Me nuclease. By determining over 40 atomic resolution structures of I-Ppol during its reaction process, we show that one and only one divalent metal ion is involved in DNA hydrolysis. Moreover, we uncover several possible deprotonation pathways for the nucleophilic water. Notably, metal ion binding and water deprotonation are highly concerted during catalysis. Our findings provide mechanistic insights into one-metal-ion-dependent nucleases, enhancing future design and engineering of these enzymes for emerging biomedical applications.

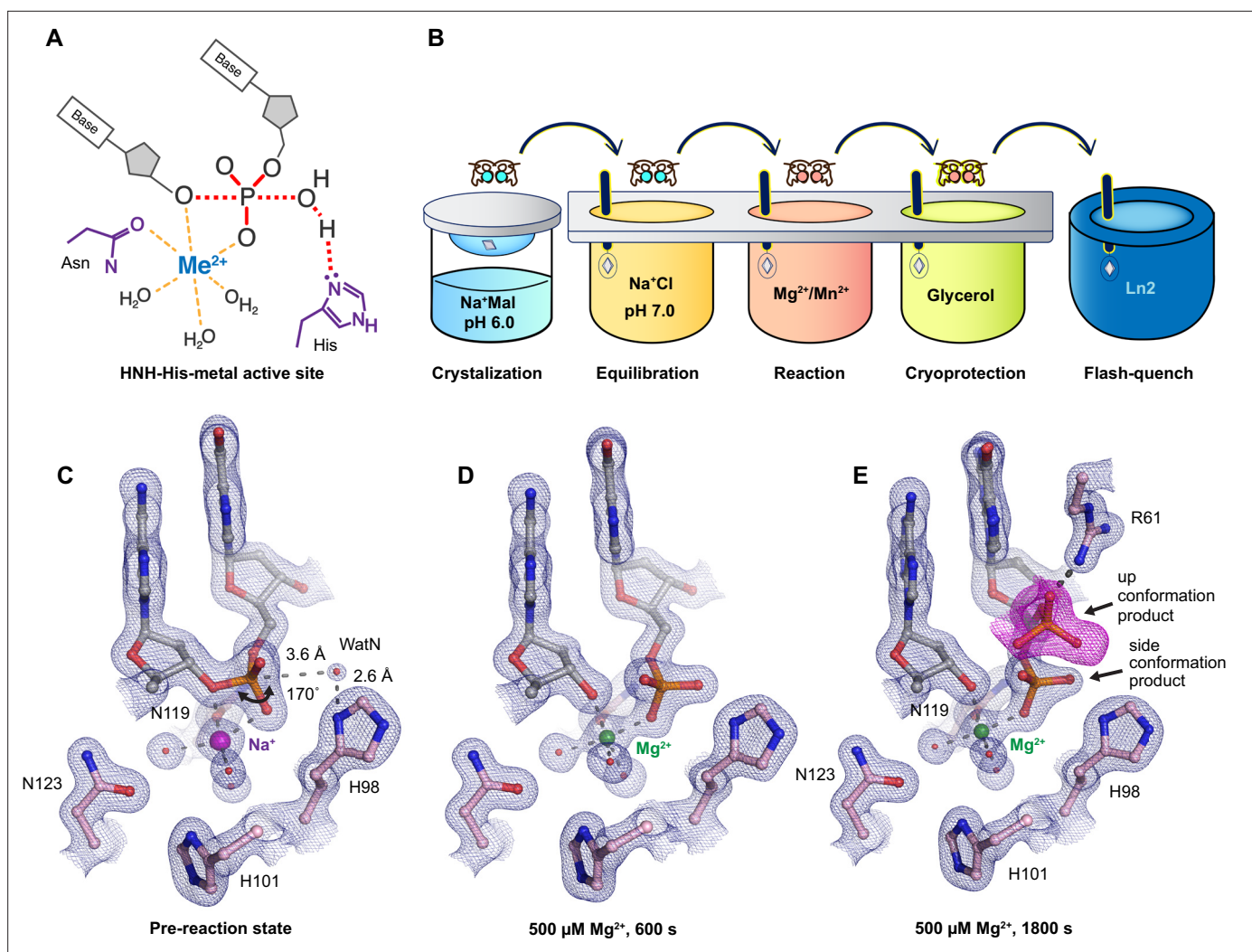


Figure 1. Observing histidine-metal (His-Me) family I-Ppol catalyze DNA hydrolysis *in crystallo*. (A) Model of one-metal-ion-dependent and histidine-promoted His-Me enzyme catalysis and transition-state stabilization. (B) Metal ion soaking setup for *in crystallo* observation of DNA hydrolysis with I-Ppol. Structural intermediates of I-Ppol *in crystallo* DNA cleavage showcasing the pre-reaction state in (C) and product states in (D) and (E). The $2F_o - F_c$ map for Me^{2+} , DNA, waters (red spheres), and catalytic residues (blue) was contoured at 2.0σ (σ values represent root mean square (r.m.s.) density values (later referred to as r.m.s.d.)). (E) The $F_o - F_c$ omit map for the up conformation of the product (violet) was contoured at 3.0σ .

The online version of this article includes the following figure supplement(s) for figure 1:

Figure supplement 1. Overall structure and catalytic core of homing endonuclease I-Ppol.

Figure supplement 2. Active sites of histidine-metal (His-Me) superfamily nucleases.

Figure supplement 3. Establishing I-Ppol for *in crystallo* studies.

Results

Preparation of the I-Ppol system for *in crystallo* DNA hydrolysis

We sought to implement I-Ppol for *in crystallo* metal ion soaking (Figure 1B), which has been successful in elucidating the catalytic mechanisms of DNA polymerases (Freudenthal et al., 2013; Gao and Yang, 2016; Nakamura et al., 2012; Vyas et al., 2015; Chim et al., 2021; Gregory et al., 2021), nucleases (Samara and Yang, 2018; Wu et al., 2019; Freudenthal et al., 2015; Whitaker et al., 2018), and glycosylase (Demir et al., 2023). First, a complex of I-Ppol and a palindromic DNA was crystallized at pH 6 with 0.2 M sodium malonate. Similar to previous studies, a dimer of I-Ppol was found in the asymmetric unit, with both active sites engaged for catalysis and DNA in the middle bent by 55° (Figure 1—figure supplement 1A). The two I-Ppol molecules were almost identical and thus served as internal controls for evaluating the reaction process (Figure 1—figure supplement

1B). Within each I-Ppol active site, a water molecule (nucleophilic water, WatN) existed 3.6 Å from the scissile phosphate, near the imidazole side chain of His98. On the leaving group side of the scissile phosphate, the metal exhibited an octahedral geometry, being coordinated by three water molecules, two oxygen atoms from the scissile phosphate, and the conserved asparagine (**Figure 1C**).

Next, we removed malonate in the crystallization buffer, which may chelate metal ions and hinder metal ion diffusion (**Deerfield et al., 1991**), by equilibrating the crystals in 200 mM NaCl buffer at pH 6, 7, or 8 for 30 min. The diffraction quality of the crystals was not affected during the soaking. The structures of I-Ppol equilibrated at pH 6, 7, or 8 in the presence of 200 mM NaCl showed no signs of product formation and appeared similar to the malonate and previous reported I-Ppol structures (**Galburt et al., 1999; Flick et al., 1998; Figure 1—figure supplement 3A**). To confirm if a monovalent metal ion binds in the pre-reaction state, we soaked the I-Ppol crystals in buffer containing Ti^+ and detected anomalous electron density at the metal ion-binding site without product formation (**Figure 1—figure supplement 3B**). Our results support that the monovalent metal ion can bind within the active site without initiating reaction, in corroboration with our biochemical assays (**Figure 1—figure supplement 3C**).

Witnessing DNA hydrolysis *in crystallo* by I-Ppol

To initiate the chemical reaction *in crystallo*, we transferred the I-Ppol crystals equilibrated in NaCl buffer to a reaction buffer with 500 μM Mg^{2+} (**Figure 1B**). After 600 s soaking, we saw a significant negative $F_o - F_c$ peak on the leaving group side of the scissile phosphate atom as well as a positive $F_o - F_c$ peak on the other side (**Figure 1—figure supplement 3D**), indicating that DNA hydrolysis was occurring *in crystallo*. After DNA cleavage, the newly generated phosphate group shifted 1 Å toward the WatN (**Figure 1D**). Furthermore, an additional product state was observed after soaking the crystals in 500 μM Mg^{2+} for 600 and 1800 s, at which the newly formed phosphate shifted 3 Å away from

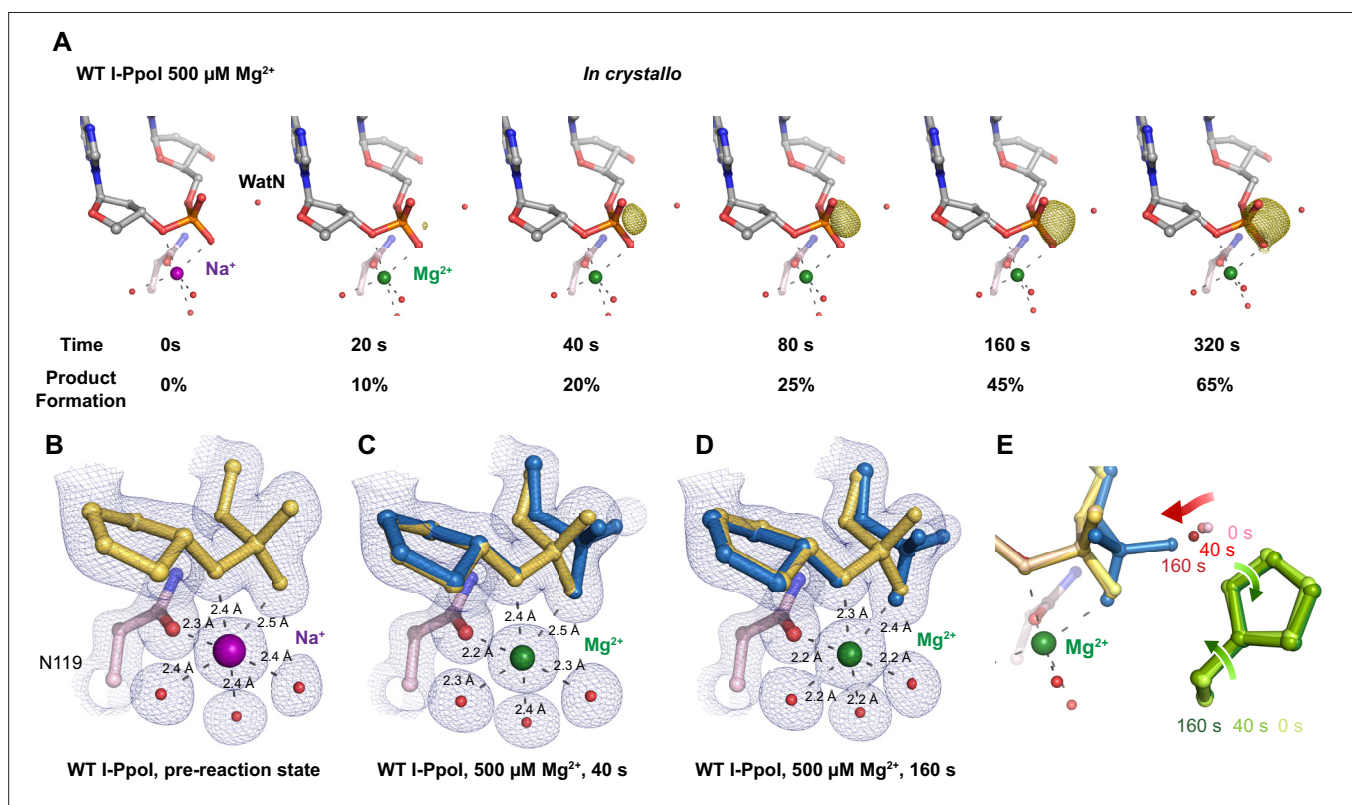


Figure 2. *In crystallo* DNA hydrolysis by I-Ppol. **(A)** Structures of I-Ppol during *in crystallo* catalysis after 500 μM Mg^{2+} soaking for 0, 20, 40, 80, 160, and 320 s. The $F_o - F_c$ omit map for the product phosphate (green) was contoured at 3.0 σ . I-Ppol complexes featuring metal ion coordination when bound with Na^+ in **(B)** Mg^{2+} in the earlier time point of the reaction process in **(C)**, and Mg^{2+} in the later time point of the reaction process in **(D)**. The $2F_o - F_c$ map for Mg^{2+} , DNA, waters (red spheres), and catalytic residues (blue) was contoured at 2.0 σ . **(E)** Alignment of the WatN and rotation in His98 during I-Ppol reaction.

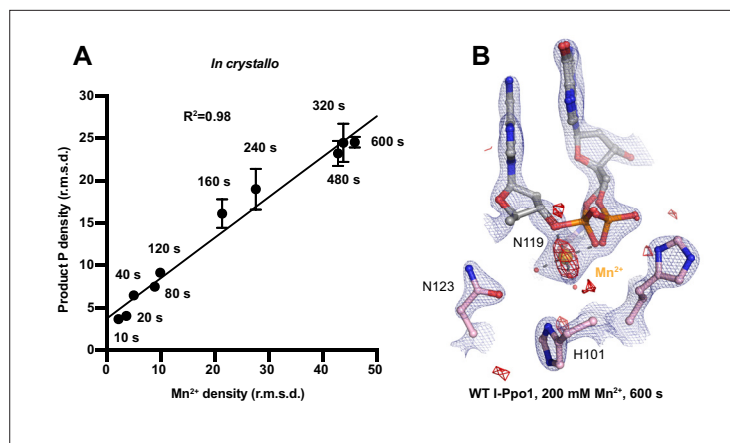


Figure 3. Detection of Me^{2+} binding during DNA hydrolysis *in crystallo*. **(A)** Correlation (R^2) between the newly formed phosphate and Mn^{2+} binding at pH 6. The points represent the mean of duplicate measurements for the electron density of the reaction product phosphate within two I-Ppo1 molecules in the asymmetric unit while the error bars represent the standard deviation. **(B)** Additional Mn^{2+} -binding sites were not detected in the I-Ppo1 active site after 10 min soaking in 200 mM Mn^{2+} . The $2F_o - F_c$ map for Me^{2+} , DNA, waters (red spheres), and catalytic residues (blue) was contoured at 2.0σ . The anomalous map for Mn^{2+} was collected at X-ray wavelength of 0.9765 \AA and contoured at 3.0σ .

The online version of this article includes the following figure supplement(s) for figure 3:

Figure supplement 1. Additional metal ions are not required for DNA hydrolysis by I-Ppo1.

Figure supplement 2. Environment of the transient Me^{2+} in nucleases.

the metal ion to form a hydrogen bond with Arg61 (**Figure 1E**). Our results confirm that the implementation of I-Ppo1 with *in crystallo* Me^{2+} soaking is feasible for observing the I-Ppo1 catalytic process and dissecting the mechanism of His-Me nucleases.

With an established *in crystallo* reaction system, we next monitored the reaction process by soaking I-Ppo1 crystals in buffer containing $500 \mu\text{M Mg}^{2+}$ pH 7, for 10–1200 s. Density between the reactant phosphate and nucleophilic water increased along with longer soaking time, indicating the generation of phosphate products (**Figure 2A**). During the reaction, the coordination distances of the metal ion ligands decreased $0.1\text{--}0.2 \text{ \AA}$ when Mg^{2+} exchanged with Na^+ , which is consistent with their preferred geometry (Cowan, 2002; **Figure 2B, C**). At reaction time 160 s, 45% of product had been generated (**Figure 2D**), which later plateaued to 65% at 300 s. During the reaction process, the sugar ring of the reactant and product DNA that resides around 3 \AA away from the scissile phosphate, remained in a C3'-endo conformation. As Mg^{2+} soaking time increased from 10 to 160 s, we observed the WatN approaching the scissile phosphate (**Figure 2E**). At the same time, the conserved His98 sidechain proposed to deprotonate the WatN was slightly rotated.

A single divalent metal ion was captured during DNA hydrolysis

Throughout the reaction process with Mg^{2+} , we found that the electron density for the Mg^{2+} metal ion strongly correlated ($R^2 = 0.97$) with product formation (**Figure 3—figure supplement 1A, C**), which may suggest that saturation of this metal ion site is required and sufficient for catalysis. However, Mg^{2+} 's similar size to Na^+ makes it suboptimal for quantifying metal ion binding. To thoroughly investigate metal ion dependence, we repeated the *in crystallo* soaking experiment with Mn^{2+} , which is more electron rich and can be unambiguously assigned based on its electron density and anomalous signal. With $500 \mu\text{M Mn}^{2+}$ in the reaction buffer, we found that the reaction process and the product conformation were similar to that for Mg^{2+} . After 160 s Mn^{2+} soaking, clear anomalous signal was present at the metal ion-binding site, confirming the binding of Mn^{2+} (**Figure 3—figure supplement 1F**). For crystal structures of I-Ppo1 with partial product formation, Mn^{2+} signal at the metal ion site correlated with product formation with a R^2 of 0.98 (**Figure 3A** and **Figure 3—figure supplement 1B**). To further search if additional and transiently bound divalent ions participate in the reaction, we soaked the I-Ppo1 crystals in high concentration of Mn^{2+} (200 mM) for 600 s, at which 80% product formed within

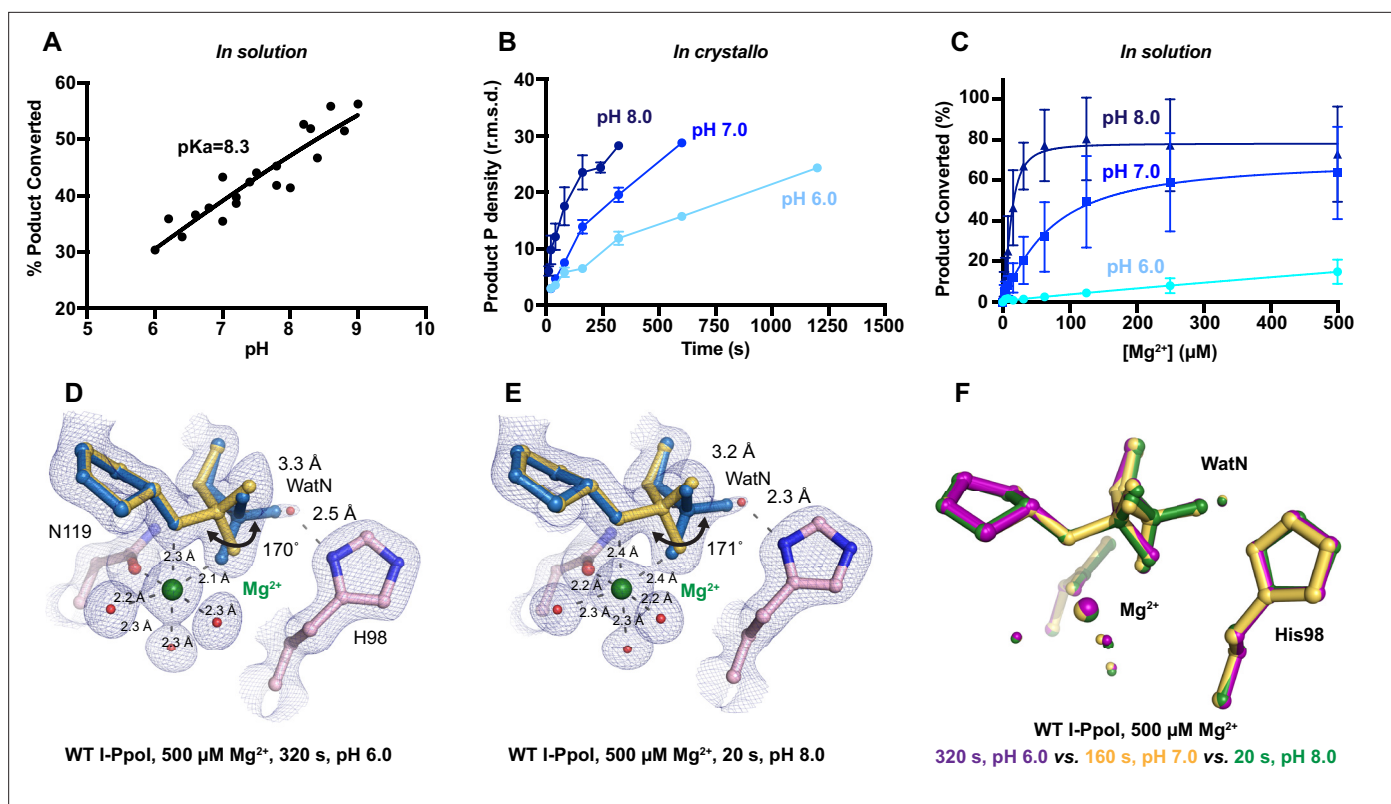


Figure 4. Effect of pH on I-Ppol DNA hydrolysis. (A) DNA hydrolysis by WT I-Ppol with increasing pH in solution. (B) DNA hydrolysis by WT I-Ppol *in crystallo* at pH 6, 7, and 8. The points represent the mean of duplicate measurements for the electron density of the reaction product phosphate after a period of Mg^{2+} soaking within two I-Ppol molecules in the asymmetric unit. The error bars represent the standard deviation. (C) The effect of pH on metal ion dependence in solution. The points represent the mean of triplicate measurements for the percentage of cleaved DNA product while the error bars represent the standard deviation. (D) Structure of I-Ppol *in crystallo* DNA hydrolysis at pH 6 after 320 s of 500 μM Mg^{2+} soaking. (E) Structure of I-Ppol *in crystallo* DNA hydrolysis at pH 8 after 20 s of 500 μM Mg^{2+} soaking. (D, E) The $2F_o - F_c$ map for Mg^{2+} , DNA, waters (red spheres), and catalytic residues (blue) was contoured at 2.0 σ . (F) Structural comparison of the active site after 500 μM Mg^{2+} soaking for 320 s at pH 6 (violet), 160 s at pH 7 (yellow), and 20 s at pH 8 (green).

the active site. However, apart from the single metal ion-binding site, we do not detect anomalous signal for additional Mn^{2+} , despite such high concentration of Mn^{2+} (Figure 3B and Figure 3—figure supplement 2). The strong correlation between product phosphate formation with Mn^{2+} binding and the absence of additional anomalous density peaks in heavy Mn^{2+} soaked crystals suggest that one and only one divalent metal ion is involved in I-Ppol DNA hydrolysis.

To examine if additional monovalent metal ions participate during DNA hydrolysis, we titrated TI^+ , which can replace monovalent Na^+ or K^+ and yields anomalous signal (Auffinger *et al.*, 2016; Kiser *et al.*, 2009), at up to 100 mM concentration in the biochemical assay. Apart from precipitation that occurred at 50 and 100 mM TI^+ , we found that product conversion remained unaffected with increasing TI^+ in solution (Figure 3—figure supplement 1G). Similarly, increasing Na^+ concentration in solution did not increase product conversion (Figure 3—figure supplement 1H). In addition, only one TI^+ was detected by its anomalous signal in the pre-reaction state (Figure 1—figure supplement 3B). The biochemical and structural results indicate that additional monovalent metal ion may not be necessary for DNA hydrolysis. However, crystal deterioration limited us from soaking the I-Ppol crystals in high concentration of TI^+ for *in crystallo* reaction.

pH dependence of I-Ppol DNA cleavage

During DNA hydrolysis, deprotonation of the WatN is required for the nucleophilic attack and phosphodiester bond breakage. This proton transfer has been proposed to be mediated by the highly conserved His98 (Galburt *et al.*, 1999; Flick *et al.*, 1998) that lies within 3 Å from the WatN. We speculated that the ability of His98 to activate the nearby WatN and mediate proton transfer would

be affected by pH. The DNA cleavage assay revealed that I-Ppol cleavage activity increased with pH with a pKa of 8.3 (Figure 4A), which is much higher than the pKa of histidine, but the histidine pKa and the proton transfer process may be affected by the active site environment. To explore how pH affects the active site configuration and catalysis, we conducted *in crystallo* soaking experiments with Mg^{2+} at pH 6 and 8 in addition to the pH 7 data series in Figure 2. Consistent with in solution experiments, higher pH resulted in faster product formation *in crystallo* (Figure 4B), indicating that metal ion binding may also be affected by pH. To test this, we performed Mg^{2+} titration at different pH in solution. Our results showed that over 100 times higher concentration of Mg^{2+} was needed to yield 50% product in pH 6 versus 8 (Figure 4C), confirming that pH affects metal-ion-dependent I-Ppol catalysis. Likewise, the reactions *in crystallo* at higher pH reached 50% product formation at shorter soaking times (320 s at pH 6, 160 s at pH 7, and 80 s at pH 8, respectively). Interestingly, the crystal

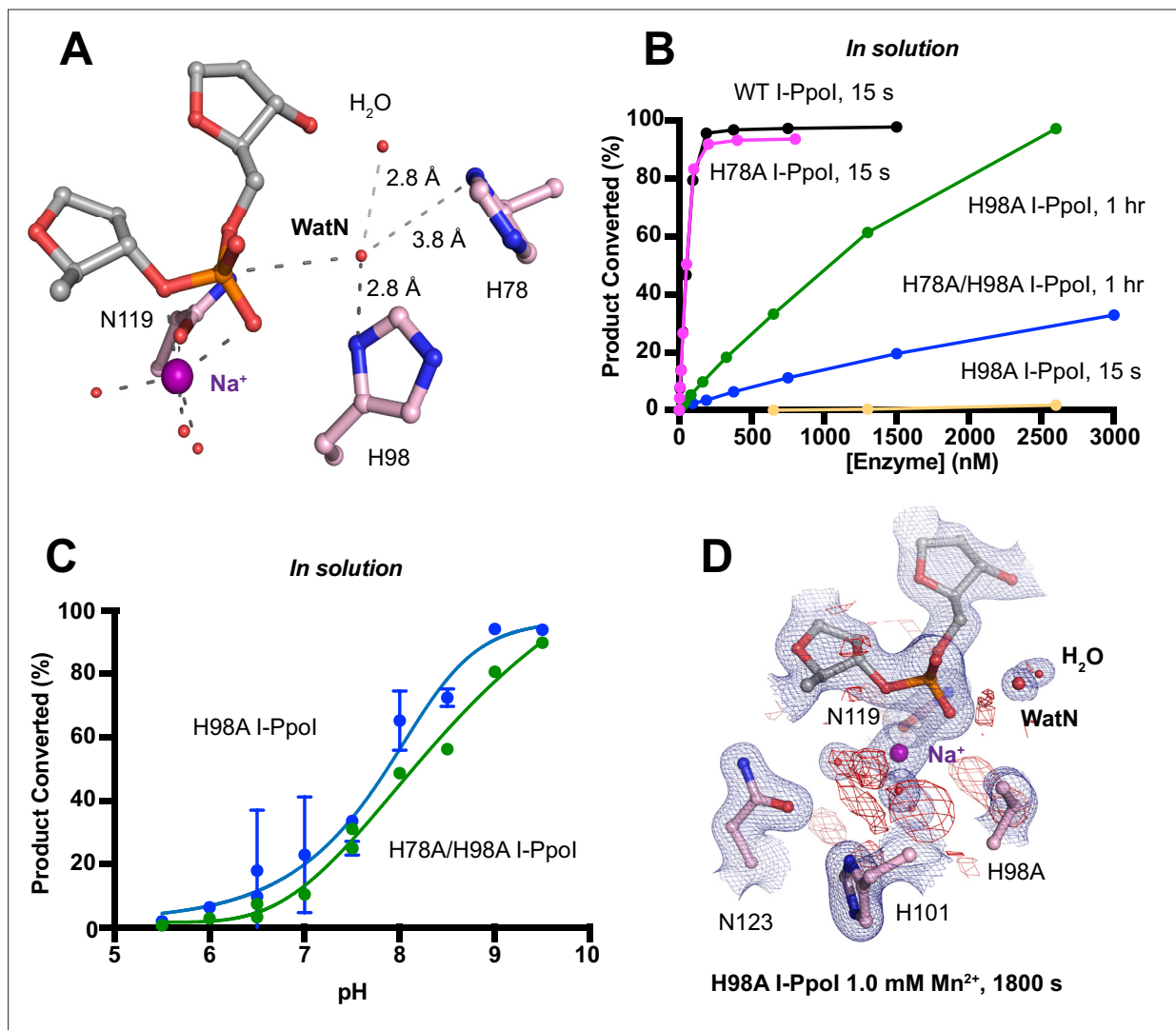


Figure 5. Nucleophilic water deprotonation during I-Ppol DNA hydrolysis. (A) Active site environment surrounding WatN. His 78 exists near the WatN besides His98. (B) In solution DNA hydrolysis activity of various I-Ppol histidine mutants. The points represent the mean of triplicate measurements for the percentage of cleaved reaction product while the error bars (too small to see) represent the standard deviation. (C) DNA hydrolysis by H98A I-Ppol (blue) and H78A/H98A I-Ppol (green) at various pH in solution. (D) Structure of H98A I-Ppol active site after 1 mM Mn^{2+} soaking for 1800s. The anomalous map for Mn^{2+} was determined at X-ray wavelength of 0.9765 Å and contoured at 2.0σ . The $2F_o - F_c$ map for Me^{2+} , DNA, waters (red spheres), and catalytic residues (blue) was contoured at 2.0σ . (B, C) The points represent the mean of triplicate measurements for the percentage of generated reaction product while the error bars represent the standard deviation.

The online version of this article includes the following figure supplement(s) for figure 5:

Figure supplement 1. Histidine I-Ppol mutants and partial rescued cleavage activity by imidazole.

structures that contained 30–35% product at pH 6 and 8 were nearly identical (**Figure 4D, E**). The positions of the His98 residue and the WatN were practically superimposable (**Figure 4F**). At all pH, Mg^{2+} binding strongly correlated with product formation ($R^2 > 0.95$), suggesting that low pH reduces the overall reaction rate without altering the reaction pathway (**Figure 3—figure supplement 1D, E**).

Nucleophilic water deprotonation pathway during I-Ppol DNA cleavage

We next investigated the deprotonation pathway with mutagenesis. Because His98 has been proposed to primarily activate the nucleophilic water, we first mutated His98 to alanine (**Figure 5A**). As expected, cleavage activity of H98A I-Ppol drastically dropped. Our assays showed that H98A I-Ppol displayed residual activity but required a reaction time of 1 hr to be comparable to WT I-Ppol (**Figure 5B**), similar to the H98Q mutant in previous studies (*Eastberg et al., 2007*). Furthermore, varying the pH resulted in a sigmoidal activity curve of I-Ppol pH dependence, corresponding to a pKa of 7.9 (**Figure 5C**). The significantly reduced reaction rate and the shift of pH dependence suggest that His98 plays a key role in pH sensing and water deprotonation. On the other hand, the low but existing activity of H98A I-Ppol suggests the presence of alternative general bases for proton transfer. Another histidine (His78) resides on the nucleophile side 3.8 Å from the WatN, with a cluster of water molecules in between (**Figure 5A**). We hypothesized that His78 may substitute His98 as the proton acceptor. The DNA cleavage assays revealed that the single mutant, H78A I-Ppol, had an activity similar to WT, whereas the double mutant (H78A/H98A I-Ppol) exhibited much lower activity than that of H98A (**Figure 5B**). Furthermore, varying the pH for H78A/H98A I-Ppol resulted in a sigmoidal activity curve that corresponded to a pKa of 8.7 (**Figure 5C**). In consistent with previous speculations, our results confirm the possibility of His78 as an alternative general base (*Eastberg et al., 2007*). The residual activity and pH dependence of H78A/H98A I-Ppol indicated that something else was still activating the nucleophilic water in the absence of any nearby histidine. Furthermore, we found that titrating imidazole in H98A and H78A/H98A I-Ppol partially rescued cleavage activity (**Figure 5—figure supplement 1A, B**), similar as observed in Cas9 and EndA nuclease (*Furuhata and Kato, 2021; Moon et al., 2011*). Collectively, our results indicate that His98 is the primary proton acceptor like previous simulation results (*Maghsoud et al., 2023*) but at the same time, I-Ppol can use alternative pathways to activate the nucleophilic WatN.

We next sought to understand the mechanism of His98-promoted hydrolysis from a structural standpoint. In our *in crystallo* soaking experiments, we equilibrated H98A I-Ppol crystals in 500 μM Mg^{2+} . The structure looked nearly identical to the Na^+ structure and previous H98A I-Ppol structure with Mg^{2+} . As shown earlier, the coordination environment of Na^+ and Mg^{2+} was quite similar. To confirm divalent metal ion binding, the H98A I-Ppol crystals were soaked for 1800s in 500 μM Mn^{2+} , the same concentration used to initiate DNA hydrolysis by WT I-Ppol. However, to our surprise, the metal ion-binding site was devoid of any anomalous signal. Increasing the Mn^{2+} concentration to 1 mM still did not produce anomalous density at the Me^{2+} -binding site (**Figure 5D** and **Figure 5—figure supplement 1C**). The results indicate that metal ion binding can be altered by perturbing His98 and possibly water deprotonation, even though the metal ion-binding site and His98 exist 7 Å apart without direct interaction. Although we tried soaking the H98A I-Ppol crystals in 1 mM Mg/Mn^{2+} and 100 mM imidazole for 15 h, metal ion binding, imidazole binding, or product formation were not detected (**Figure 5—figure supplement 1D**), possibly due to the difficulty of imidazole diffusion within the lattice. Our results indicate that perturbing the deprotonation pathway not only affects nucleophilic attack but also metal binding, suggesting that I-Ppol catalyzes DNA catalysis via a concerted mechanism.

Discussion

Time-resolved crystallography can visualize time-dependent structural changes and elucidate mechanisms of enzyme catalysis with unparalleled detail *in crystallo*, especially for light-dependent enzymes, in which the reactions can be synchronously initiated by light pulses (*Wilson, 2022; Brändén and Neutze, 2021; Maestre-Reyna et al., 2023; Christou et al., 2023*). In complementary, recently advanced metal ion diffusion-based time-resolved crystallographic techniques have uncovered rich dynamics at the active site and transient metal ion binding during the catalytic processes of metal-ion-dependent DNA polymerases (*Freudenthal et al., 2013; Gao and Yang, 2016; Nakamura et al.,*

2012; Vyas *et al.*, 2015; Chim *et al.*, 2021; Gregory *et al.*, 2021), nucleases (Samara and Yang, 2018; Wu *et al.*, 2019), and glycosylase (Demir *et al.*, 2023). In addition to metal ions captured in static structures, these transient metal ions have been shown to play critical roles in catalysis, such as water deprotonation for nucleophilic attack in RNaseH (Samara and Yang, 2018), bond breakage and product stabilization in polymerases (Freudenthal *et al.*, 2013; Gao and Yang, 2016; Nakamura *et al.*, 2012; Vyas *et al.*, 2015; Gregory *et al.*, 2021; Reed and Suo, 2017; Chang *et al.*, 2022), and alignment of the substrate and nucleophilic water in MutT (Nakamura and Yamagata, 2022). Interestingly, one and only one metal ion was captured within the I-Ppol active site during catalysis, even when high concentration (200 mM Mn^{2+}) of metal ion was tested (Figure 3). The observed location of the Me^{2+} on the leaving group side of the scissile phosphate corresponds to the Me^{2+}_b in two-metal-ion-dependent nucleases (Yang, 2008; Figure 1—figure supplement 2). However, the metal ion is unique in its environment and role. First, it is coordinated by a water cluster and asparagine side chain (sometimes with an additional aspartate residue) rather than the acidic aspartate and glutamic acid clusters that outline the active sites of RNaseH and APE1 nuclease (Tsutakawa *et al.*, 2013) as well as DNA polymerases (Figure 6—figure supplement 1). Even in the absence of divalent Mg^{2+} or Mn^{2+} , the active site including the scissile phosphate was already well aligned in I-Ppol, which is again different from RNaseH. Instead, Leu116 and the beta sheet consisting of Arg61, Gln63, Lys65, and Thr67 (Flick *et al.*, 1998; Galburt *et al.*, 2000) helped to position the DNA optimally toward the active site (Figure 1—figure supplement 1A, C). Second, single metal ion binding is strictly correlated with product formation in all conditions, at different pH and with different mutants (Figure 3A and Figure 3—figure supplement 1A–E; Moon *et al.*, 2011). Thus, similar to the third metal ion in DNA polymerases and RNaseH, the metal ion in I-Ppol is not required for substrate alignment but is essential for catalysis. We suspect that the single metal ion helps stabilize the transition state and reduce the electronegative buildup of DNA, thereby promoting DNA hydrolysis.

Proton transfer by a general base is essential for a SN_2 -type nucleophilic attack. Such deprotonation of the nucleophilic water has been attributed to His98, which is highly conserved in His-Me nucleases. Existing close to the nucleophilic water at 2.6 Å, His98 is perfectly positioned to mediate the proton transfer. Moreover, due to the bulky presence of His98 and beta sheet protein residues, there is no space for an additional metal ion at the nucleophilic side (Figure 3—figure supplement

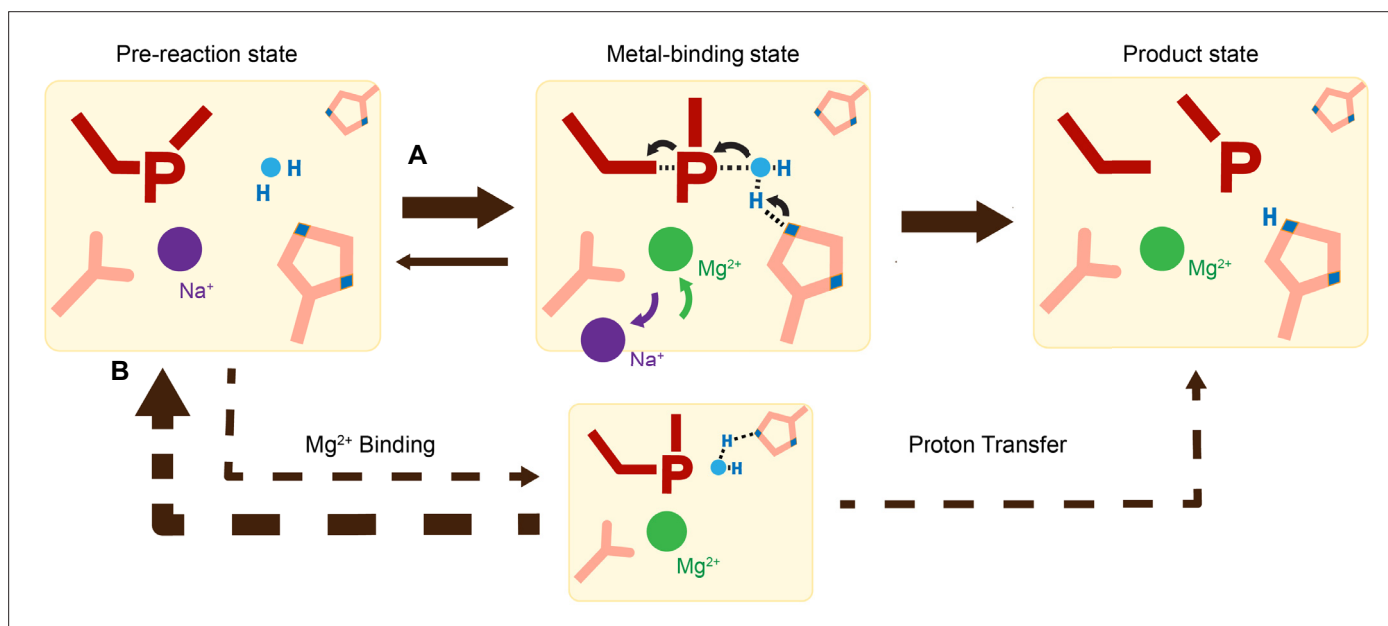


Figure 6. Catalytic model of histidine-metal (His-Me) nuclease DNA hydrolysis. Proposed model of His-Me nuclease DNA hydrolysis in which Me^{2+} binding, proton transfer, and nucleophilic attack are concerted (solid arrow) in the presence of the primary proton acceptor in (A) versus unfavored (dashed arrows) in the absence of the primary proton acceptor in (B).

The online version of this article includes the following figure supplement(s) for figure 6:

Figure supplement 1. Active sites of Me^{2+} -binding enzymes.

2). The H98A mutation significantly reduced catalytic activity and altered pH dependence. But since H98A I-Ppol showed residual activity, His78, imidazole, or its surrounding waters may still serve as alternative general bases for accepting the proton, similar to Pol η , in which primer 3'-OH deprotonation can occur through multiple pathways (Gregory *et al.*, 2021). However, the order of events regarding metal ion binding, water deprotonation, and nucleophilic attack remains unanswered. Based on our *in crystallo* observations, water deprotonation and metal ion binding appeared to be highly correlated (Figure 6A). Lowering the pH not only reduced reaction rate but also slowed metal ion binding (Figure 4B, C). Moreover, the metal ion was not observed *in crystallo* when His98 was removed (Figure 5D). As there is no direct interaction between His98 and the Mg^{2+} -binding site, the divalent metal ion may be sensitive to the charge potential of the substrate scissile phosphate, which may be indirectly affected by the deprotonated state of the nucleophilic water. Conversely, binding of the divalent metal ion may alter the local electrostatic environment and affect His98 deprotonation. Consistently, previous molecular dynamics simulation of Cas9 has suggested that the histidine pKa is highly sensitive to active site changes (Nierzwicki *et al.*, 2022). Without a proper proton acceptor, the metal ion may be prone for dissociation without the reaction proceeding, and thus stable Mg^{2+} binding was not observed *in crystallo* without His98 (Figure 6B). On the other hand, optimal alignment of the metal ion and WatN within the active site, labeled as metal-binding state, leads to irreversible bond breakage (Figure 6A). In summary, our experimental observations suggest a concerted mechanism for one-metal-ion promoted DNA hydrolysis, offering guidance for future computational analysis of enzyme catalysis (Nierzwicki *et al.*, 2022) and the rational design and engineering of nucleases (Ashworth *et al.*, 2006) for biotechnological and biomedical applications.

Materials and methods

Protein expression and purification

WT, His78Ala, His98Ala, and H78A/H98A *physarum polycephalum* I-Ppol (residues 1–162) were cloned into a modified pET28p vector with a N-terminal 6-histidine tag and a PreScission Protease cleavage site. For protein expression, this I-Ppol plasmid was transformed into BL21 DE3 *E. coli* cells, which were grown in a buffer that contained (10 g/l glucose, 40 g/l α -lactose, 10% glycerol) for 24 hr (20°C). The cell paste was collected via centrifugation and re-suspended in a buffer that contained 50 mM Tris (pH 7.5), 1 M NaCl, 1 mM MgCl_2 , 10 mM imidazole, 2 mM β -mercaptoethanol (BME), and 5% glycerol. After sonification, I-Ppol was loaded onto a HisTrap HP column (GE Healthcare), which was pre-equilibrated with a buffer that contained 50 mM Tris (pH 7.5), 1 M NaCl, 1 mM MgCl_2 , 10 mM imidazole, 2 mM BME, and 5% glycerol. The column was washed with 300 ml of buffer to remove non-specific bound proteins and was eluted with buffer that contained 50 mM Tris (pH 7.5), 1 M NaCl, 1 mM MgCl_2 , 300 mM imidazole, and 2 mM BME. The eluted I-Ppol was incubated with PreScission Protease to cleave the N-terminal 6-histidine-tag. Afterwards, I-Ppol was desalted to 50 mM Tris (pH 7.5), 167 mM NaCl, 1 mM MgCl_2 , 2 mM BME, and 5% glycerol and was loaded onto a Heparin column (GE Healthcare) equilibrated with 50 mM Tris (pH 7.5) and 167 mM NaCl. The protein was eluted with an increasing salt (NaCl) gradient, concentrated, and stored at 40% glycerol at -80°C .

DNA hydrolysis assays

DNA hydrolysis activity of varying time was assayed by the following: The reaction mixture contained 100 nM WT I-Ppol, 50 mM NaCl, 100 mM Tris (pH 7.5), 1.5 mM dithiothreitol (DTT), 0.05 mg/ml bovine serum albumin (BSA), 50 nM DNA, 10 μM ethylenediaminetetraacetic acid (EDTA), and 4% glycerol. The hydrolysis assays were executed using a palindromic 5'-fluorescein-labeled DNA duplex (5'-TTG ACT CTC TTA AGA GAG TCA-3'). Reactions were initiated by adding 10 mM MgCl_2 to the reaction mixture for 0–1 hr at 37°C and were stopped by mixing with equal volume of a quench buffer, which contain 80% formamide, 100 mM EDTA (pH 8.0), 0.2 mg/ml xylene cyanol, and 0.2 mg/ml bromophenol.

The DNA hydrolysis activity at different pH was assayed by the following: The reaction mixture contained 100–3000 nM WT, H98A, and H78A/H98A I-Ppol, 50 mM NaCl, 1.5 mM DTT, 0.05 mg/ml BSA, 50 nM DNA, 10 μM EDTA, and 4% glycerol. Reactions were initiated by adding 50 mM 2-(N-morpholino)ethanesulfonic acid (MES) (pH 5.5–6.5), 50 mM 4-(2-hydroxyethyl)-1-piperazineetha

nesulfonic acid (HEPES) (pH 6.5–7.5), or 50 mM Tris (pH 7.5–9.5) together with 10 mM MgCl_2 to the reaction mixture for 30 min at 37°C and were stopped by adding equal volume of quench buffer.

The DNA hydrolysis activity with different mutants was assayed by the following: The reaction mixture contained 50 mM NaCl, 100 mM Tris (pH 7.5), 1.5 mM DTT, 0.05 mg/ml BSA, 50 nM DNA, 10 mM MgCl_2 , 10 μM EDTA, and 4% glycerol. Reactions were initiated by adding 0–3000 nM of WT, H78A, H98A, H78A/H98A I-Ppol to the reaction mixture for 15 s or 1 hr at 37°C and stopped by adding equal volume of quench buffer.

The DNA hydrolysis activity with different metal ions was assayed by the following: The reaction mixture contained 100 nM WT I-Ppol, 50 mM NaCl, 100 mM Tris (pH 7.5), 1.5 mM DTT, 0.05 mg/ml BSA, 50 nM DNA, 10 μM EDTA, and 4% glycerol. Reactions were initiated by adding 10 mM of MgCl_2 , MnCl_2 , CaCl_2 , NiCl_2 , and ZnCl_2 to the reaction mixture for 15 s at 37°C and were stopped by adding equal volume of quench buffer.

The DNA hydrolysis activity with Tl^+ or additional Na^+ was assayed by the following: The reaction mixture contained 100–3000 nM WT I-Ppol, 100 mM Tris (pH 7.5), 1.5 mM DTT, 0.05 mg/ml BSA, 50 nM DNA, 10 μM EDTA, and 4% glycerol. Reactions were conducted at 37°C for 30 min by adding 0–350 mM TlCl or NaCl together with 10 mM MgCl_2 to the reaction mixture and were stopped by adding equal volume of quench buffer.

The DNA hydrolysis activity with imidazole was assayed by the following: The reaction mixture contained 100–3000 nM H98A and H78A/H98A I-Ppol, 50 mM NaCl, 100 mM Tris (pH 7.5), 1.5 mM DTT, 0.05 mg/ml BSA, 50 nM DNA, 10 μM EDTA, and 4% glycerol. Reactions were conducted at 37°C for 30 min by adding 0–100 mM imidazole together with 10 mM MgCl_2 to the reaction mixture and were stopped by adding equal volume of quench buffer.

For all reactions, after heating the quenched reaction mix to 97°C for 5 min and immediately placing on ice, reaction products were resolved on 22.5% polyacrylamide urea gels. The gels were visualized by a Sapphire Biomolecular Imager and quantified using the built-in software. Quantification of percentage cleaved and graphic representation were executed by Graph Prism.

Crystallization

WT or H98A I-Ppol in a buffer containing 20 mM Tris 7.5, 300 mM NaCl, 3 mM DTT, and 0.1 mM EDTA was added with (5'-TTG ACT CTC TTA AGA GAG TCA-3') DNA at a molar ratio of 1:1.5 for I-Ppol and DNA and added with threefold volume of buffer that contained 20 mM Tris 7.5, 3 mM DTT, and 0.1 mM EDTA. This I-Ppol–DNA complex was then cleaned with a Superdex 200 10/300 GL column (GE Healthcare) with a buffer that contained 20 mM Tris 7.5, 150 mM NaCl, 3 mM DTT, and 0.1 mM EDTA. The I-Ppol–DNA complex was concentrated to 2.8 mg/ml I-Ppol (confirmed by Bradford assay). All crystals were obtained using the hanging-drop vapor-diffusion method against a reservoir solution containing 0.1 M MES (pH 6.0), 0.2 M sodium malonate, and 20% (wt/vol) PEG3350 at room temperature within 4 days.

To identify the monovalent Me^+ species that binds during the pre-reaction state, WT I-Ppol crystals were transferred and incubated in a buffer containing 0.1 M MES (pH 6.0), 70 mM thallium acetate and 20% (wt/vol) PEG3350 for 30 min. Afterwards, the crystals were quickly dipped in a cryo-solution supplemented with 20% (wt/vol) glycerol and flash-cooled in liquid nitrogen.

Chemical reaction *in crystallo*

The WT I-Ppol crystals were first transferred and incubated in a pre-reaction buffer containing 0.1 M MES (pH 6.0 or 7.0) or 0.1 M Tris (pH 8.0), 0.2 M NaCl, and 20% (wt/vol) PEG3350 for 30 min. The chemical reaction was initiated by transferring the crystals into a reaction buffer containing 0.1 M MES (pH 6.0 or 7.0) or 0.1 M Tris (pH 8.0), 0.2 M NaCl, and 20% (wt/vol) PEG3350, and 500 μM MgCl_2 or MnCl_2 . After incubation for a desired time period, the crystals were quickly dipped in a cryo-solution supplemented with 20% (wt/vol) glycerol and flash-cooled in liquid nitrogen.

To observe any additional Me^{2+} binding sites during DNA hydrolysis, WT I-Ppol crystals were first transferred and incubated in a pre-reaction buffer containing 0.1 M MES (pH 6.0), 0.2 M NaCl, and 20% (wt/vol) PEG3350 for 30 min. The chemical reaction was initiated by transferring the crystals into a reaction buffer containing 0.1 M MES (pH 6.0), 0.2 M NaCl, and 20% (wt/vol) PEG3350, and 200 mM MnCl_2 . After incubation for 600 s, the crystals were quickly dipped in a cryo-solution supplemented with 20% (wt/vol) glycerol and flash-cooled in liquid nitrogen.

The metal ion soaking experiments with His98Ala I-Ppol were performed following the similar protocol as that of WT I-Ppol. His98Ala I-Ppol crystals were first incubated in a pre-reaction buffer containing 0.1 M MES 7.0, 0.2 M NaCl, and 20% (wt/vol) PEG3350 for 30 min, followed by 1800s incubation in a reaction buffer containing 0.1 M MES 7.0, 0.2 M NaCl, and 20% (wt/vol) PEG3350, and 1 mM MnCl₂. To observe whether soaking in imidazole can initiate the reaction in the absence of His98, His98Ala I-Ppol crystals were first transferred and incubated in a buffer containing 0.1 M MES (pH 6.0), 0.2 M NaCl, 1 mM MnCl₂, and 20% (wt/vol) PEG3350 for 30 min. The crystals were then transferred into a reaction buffer containing 0.1 M MES (pH 6.0), 0.2 M NaCl, 1 mM MgCl₂ or MnCl₂, and 100 mM imidazole, and 20% (wt/vol) PEG3350. After incubation for a desired time period, the crystals were quickly dipped in a cryo-solution supplemented with 20% (wt/vol) glycerol and flash-cooled in liquid nitrogen.

Data collection and refinement

Diffraction data were collected at 100 K on LS-CAT beam lines 21-D-D, 21-ID-F, and 21-ID-G at 1.1 or 0.97 Å at the Advanced Photon Source (Argonne National Laboratory) or beamlines 5.0.3 at 0.97 Å at Advanced Light Source (ALS). Data were indexed in space group P3₁21, scaled with XSCALE and reduced using X-ray Detector Software (XDS) (Kabsch, 2010). Isomorphous I-Ppol structures with Na⁺ PDB ID 1CZ0 were used as initial models for refinement using PHENIX (Adams et al., 2010) and COOT (Emsley et al., 2010).

Occupancies were assigned for the reaction product until there were no significant $F_o - F_c$ peaks. Occupancies were assigned for the metal ions, following the previous protocol (Gao and Yang, 2016) until (1) there were no significant $F_o - F_c$ peaks, (2) the B value had roughly similar values to its ligand (3) it matched the occupancy of the reaction product. For the structures in which some $F_o - F_c$ peaks were present around the Me²⁺ binding sites or reaction product, no change in the assigned occupancy was executed when a 10% change in occupancy (e.g. 100–90%) failed to significantly change the intensity of the $F_o - F_c$ peaks. Source data of the electron densities in r.m.s. density are provided as a Source Data file. Each structure was refined to the highest resolution data collected, which ranged between 1.42 and 2.2 Å. Software applications used in this project were compiled and configured by SBGrid (Morin et al., 2013). Source data of data collection and refinement statistics are summarized in **Supplementary file 1**. All structural figures were drawn using PyMOL (<https://www.pymol.org/>).

Calculation of electron density

Electron density (r.m.s.d.) from the $F_o - F_c$ map of the product phosphate and Me²⁺ were calculated by running a round of B -factor refinement in PHENIX after omitting the reaction product phosphate and Me²⁺ atoms from phase calculation in COOT. All structures from the same experiment (Mg²⁺-pH 6.0, Mg²⁺-pH 7.0, Mg²⁺-pH 8.0, Mn²⁺-pH 6.0) were refined to the lowest resolution in the same experiment group (1.80 Å for Mg²⁺-pH 6.0, 1.59 Å for Mg²⁺-pH 7.0, 1.70 Å for Mg²⁺-pH 8.0, and 1.80 Å for Mn²⁺-pH 6.0).

Acknowledgements

Our sincere appreciation to the members of the Gao lab, and Drs. Phillips, Nikonowicz, and Lu who serve on CC's thesis committee. We thank the APS LS-CAT beam technicians and research scientists Drs. Anderson, Wawrzak, Brunzelle, and Focia. This research used resources of the Advanced Photon Source, a U.S. Department of Energy (DOE) Office of Science User Facility operated for the DOE Office of Science by Argonne National Laboratory under Contract No. DE-AC02-06CH11357. Use of the LS-CAT Sector 21 was supported by the Michigan Economic Development Corporation and the Michigan Technology Tri-Corridor (Grant 085P1000817). The Berkeley Center for Structural Biology is supported in part by the Howard Hughes Medical Institute. The Advanced Light Source is a Department of Energy Office of Science User Facility under Contract No. DE-AC02-05CH11231. The Pilatus detector on 5.0.1 was funded under NIH grant S10OD021832. The ALS-ENABLE beamlines are supported in part by the National Institutes of Health, National Institute of General Medical Sciences, grant P30 GM124169. This work is supported by CPRIT (RR190046) and the Welch Foundation (C-2033-20200401) to YG, a predoctoral fellowship from the Houston Area Molecular Biophysics Program (NIH Grant No. T32 GM008280, Program Director Dr. Theodore Wensel) to CC.

Additional information

Funding

Funder	Grant reference number	Author
Cancer Prevention and Research Institute of Texas	RR190046	Yang Gao
Welch Foundation	C-2033- 624 20200401	Yang Gao
National Institutes of Health	T32 GM008280	Caleb Chang

The funders had no role in study design, data collection, and interpretation, or the decision to submit the work for publication.

Author contributions

Caleb Chang, Conceptualization, Data curation, Formal analysis, Funding acquisition, Investigation, Writing - original draft, Writing - review and editing; Grace Zhou, Data curation, Writing - original draft; Yang Gao, Conceptualization, Funding acquisition, Writing - original draft, Writing - review and editing

Author ORCIDiDs

Caleb Chang  <http://orcid.org/0000-0002-4507-659X>

Grace Zhou  <https://orcid.org/0009-0009-9021-8305>

Yang Gao  <https://orcid.org/0000-0002-4037-0431>

Peer review material

Reviewer #1 (Public Review): <https://doi.org/10.7554/eLife.99960.3.sa1>

Reviewer #2 (Public Review): <https://doi.org/10.7554/eLife.99960.3.sa2>

Author response <https://doi.org/10.7554/eLife.99960.3.sa3>

Additional files

Supplementary files

- Supplementary file 1. Crystal diffraction and refinement data.
- MDAR checklist

Data availability

The coordinates, density maps, and structure factors for all the structures have been deposited in Protein Data Bank (PDB) under accession codes: 8VMO, 8VMP, 8VMQ, 8VMR, 8VMS, 8VMT, 8VMU, 8VMV, 8VMW, 8VMX, 8VMY, 8VMZ, 8VN0, 8VN1, 8VN2, 8VN3, 8VN4, 8VN5, 8VN6, 8VN7, 8VN8, 8VN9, 8VNA, 8VNB, 8VNC, 8VND, 8VNE, 8VNF, 8VNG, 8VNH, 8VNJ, 8VNK, 8VNL, 8VNM, 8VNN, 8VNO, 8VNP, 8VNQ, 8VNR, 8VNS, 8VNT, and 8VNU. All data are available in the main text or the supplementary materials.

The following datasets were generated:

Author(s)	Year	Dataset title	Dataset URL	Database and Identifier
Chang C, Gao Y	2024	Homing endonuclease I-Ppol-DNA complex:ground state at pH7.0 (K+ MES) with Na+	https://www.rcsb.org/structure/8VMO	RCSB Protein Data Bank, 8VMO
Chang C, Gao Y	2024	Homing endonuclease I-Ppol-DNA complex:reaction at pH7.0 (K+ MES) with 500 uM Mg2+ for 10s	https://www.rcsb.org/structure/8VMP	RCSB Protein Data Bank, 8VMP

Continued on next page

Continued

Author(s)	Year	Dataset title	Dataset URL	Database and Identifier
Chang C, Gao Y	2024	Homing endonuclease I-Ppol-DNA complex:reaction at pH7.0 (K+ MES) with 500 uM Mg2+ for 20s	https://www.rcsb.org/structure/8VMQ	RCSB Protein Data Bank, 8VMQ
Chang C, Gao Y	2024	Homing endonuclease I-Ppol-DNA complex:reaction at pH7.0 (K+ MES) with 500 uM Mg2+ for 40s	https://www.rcsb.org/structure/8VMR	RCSB Protein Data Bank, 8VMR
Chang C, Gao Y	2024	Homing endonuclease I-Ppol-DNA complex:reaction at pH7.0 (K+ MES) with 500 uM Mg2+ for 80s	https://www.rcsb.org/structure/8VMS	RCSB Protein Data Bank, 8VMS
Chang C, Gao Y	2024	Homing endonuclease I-Ppol-DNA complex:reaction at pH7.0 (K+ MES) with 500 uM Mg2+ for 160s	https://www.rcsb.org/structure/8VMT	RCSB Protein Data Bank, 8VMT
Chang C, Gao Y	2024	Homing endonuclease I-Ppol-DNA complex:reaction at pH7.0 (K+ MES) with 500 uM Mg2+ for 320s	https://www.rcsb.org/structure/8VMU	RCSB Protein Data Bank, 8VMU
Chang C, Gao Y	2024	Homing endonuclease I-Ppol-DNA complex:reaction at pH7.0 (K+ MES) with 500 uM Mg2+ for 600s	https://www.rcsb.org/structure/8VMV	RCSB Protein Data Bank, 8VMV
Chang C, Gao Y	2024	Homing endonuclease I-Ppol-DNA complex:ground state at pH6.0 (K+ MES) with Na+	https://www.rcsb.org/structure/8VMW	RCSB Protein Data Bank, 8VMW
Chang C, Gao Y	2024	Homing endonuclease I-Ppol-DNA complex:reaction at pH6.0 (K+ MES) with 500 uM Mg2+ for 10s	https://www.rcsb.org/structure/8VMX	RCSB Protein Data Bank, 8VMX
Chang C, Gao Y	2024	Homing endonuclease I-Ppol-DNA complex:reaction at pH6.0 (K+ MES) with 500 uM Mg2+ for 20s	https://www.rcsb.org/structure/8VMY	RCSB Protein Data Bank, 8VMY
Chang C, Gao Y	2024	Homing endonuclease I-Ppol-DNA complex:reaction at pH6.0 (K+ MES) with 500 uM Mg2+ for 40s	https://www.rcsb.org/structure/8VMZ	RCSB Protein Data Bank, 8VMZ
Chang C, Gao Y	2024	Homing endonuclease I-Ppol-DNA complex:reaction at pH6.0 (K+ MES) with 500 uM Mg2+ for 80s	https://www.rcsb.org/structure/8VN0	RCSB Protein Data Bank, 8VN0
Chang C, Gao Y	2024	Homing endonuclease I-Ppol-DNA complex:reaction at pH6.0 (K+ MES) with 500 uM Mg2+ for 160s	https://www.rcsb.org/structure/8VN1	RCSB Protein Data Bank, 8VN1

Continued on next page

Continued

Author(s)	Year	Dataset title	Dataset URL	Database and Identifier
Chang C, Gao Y	2024	Homing endonuclease I-Ppol-DNA complex:reaction at pH6.0 (K+ MES) with 500 uM Mg2+ for 320s	https://www.rcsb.org/structure/8VN2	RCSB Protein Data Bank, 8VN2
Chang C, Gao Y	2024	Homing endonuclease I-Ppol-DNA complex:reaction at pH6.0 (K+ MES) with 500 uM Mg2+ for 600s	https://www.rcsb.org/structure/8VN3	RCSB Protein Data Bank, 8VN3
Chang C, Gao Y	2024	Homing endonuclease I-Ppol-DNA complex:reaction at pH6.0 (K+ MES) with 500 uM Mg2+ for 1200s	https://www.rcsb.org/structure/8VN4	RCSB Protein Data Bank, 8VN4
Chang C, Gao Y	2024	Homing endonuclease I-Ppol-DNA complex:ground state at pH8.0 (Tris) with Na+	https://www.rcsb.org/structure/8VN5	RCSB Protein Data Bank, 8VN5
Chang C, Gao Y	2024	Homing endonuclease I-Ppol-DNA complex:reaction at pH8.0 (Tris) with 500 uM Mg2+ for 10s	https://www.rcsb.org/structure/8VN6	RCSB Protein Data Bank, 8VN6
Chang C, Gao Y	2024	Homing endonuclease I-Ppol-DNA complex:reaction at pH8.0 (Tris) with 500 uM Mg2+ for 20s	https://www.rcsb.org/structure/8VN7	RCSB Protein Data Bank, 8VN7
Chang C, Gao Y	2024	Homing endonuclease I-Ppol-DNA complex:reaction at pH8.0 (Tris) with 500 uM Mg2+ for 40s	https://www.rcsb.org/structure/8VN8	RCSB Protein Data Bank, 8VN8
Chang C, Gao Y	2024	Homing endonuclease I-Ppol-DNA complex:reaction at pH8.0 (Tris) with 500 uM Mg2+ for 80s	https://www.rcsb.org/structure/8VN9	RCSB Protein Data Bank, 8VN9
Chang C, Gao Y	2024	Homing endonuclease I-Ppol-DNA complex:reaction at pH8.0 (Tris) with 500 uM Mg2+ for 160s	https://www.rcsb.org/structure/8VNA	RCSB Protein Data Bank, 8VNA
Chang C, Gao Y	2024	Homing endonuclease I-Ppol-DNA complex:reaction at pH8.0 (Tris) with 500 uM Mg2+ for 240s	https://www.rcsb.org/structure/8VNB	RCSB Protein Data Bank, 8VNB
Chang C, Gao Y	2024	Homing endonuclease I-Ppol-DNA complex:reaction at pH8.0 (Tris) with 500 uM Mg2+ for 320s	https://www.rcsb.org/structure/8VNC	RCSB Protein Data Bank, 8VNC
Chang C, Gao Y	2024	Homing endonuclease I-Ppol-DNA complex:reaction at pH8.0 (Tris) with 500 uM Mg2+ for 600s	https://www.rcsb.org/structure/8VND	RCSB Protein Data Bank, 8VND

Continued on next page

Continued

Author(s)	Year	Dataset title	Dataset URL	Database and Identifier
Chang C, Gao Y	2024	Homing endonuclease I-Ppol-DNA complex:reaction at pH6.0 (K+ MES) with 500 uM Mn2+ for 10s	https://www.rcsb.org/structure/8VNE	RCSB Protein Data Bank, 8VNE
Chang C, Gao Y	2024	Homing endonuclease I-Ppol-DNA complex:reaction at pH6.0 (K+ MES) with 500 uM Mn2+ for 20s	https://www.rcsb.org/structure/8VNF	RCSB Protein Data Bank, 8VNF
Chang C, Gao Y	2024	Homing endonuclease I-Ppol-DNA complex:reaction at pH6.0 (K+ MES) with 500 uM Mn2+ for 40s	https://www.rcsb.org/structure/8VNG	RCSB Protein Data Bank, 8VNG
Chang C, Gao Y	2024	Homing endonuclease I-Ppol-DNA complex:reaction at pH6.0 (K+ MES) with 500 uM Mn2+ for 80s	https://www.rcsb.org/structure/8VNH	RCSB Protein Data Bank, 8VNH
Chang C, Gao Y	2024	Homing endonuclease I-Ppol-DNA complex:reaction at pH6.0 (K+ MES) with 500 uM Mn2+ for 120s	https://www.rcsb.org/structure/8VNJ	RCSB Protein Data Bank, 8VNJ
Chang C, Gao Y	2024	Homing endonuclease I-Ppol-DNA complex:reaction at pH6.0 (K+ MES) with 500 uM Mn2+ for 160s	https://www.rcsb.org/structure/8VNK	RCSB Protein Data Bank, 8VNK
Chang C, Gao Y	2024	Homing endonuclease I-Ppol-DNA complex:reaction at pH6.0 (K+ MES) with 500 uM Mn2+ for 240s	https://www.rcsb.org/structure/8VNL	RCSB Protein Data Bank, 8VNL
Chang C, Gao Y	2024	Homing endonuclease I-Ppol-DNA complex:reaction at pH6.0 (K+ MES) with 500 uM Mn2+ for 320s	https://www.rcsb.org/structure/8VNM	RCSB Protein Data Bank, 8VNM
Chang C, Gao Y	2024	Homing endonuclease I-Ppol-DNA complex:reaction at pH6.0 (K+ MES) with 500 uM Mn2+ for 480s	https://www.rcsb.org/structure/8VNN	RCSB Protein Data Bank, 8VNN
Chang C, Gao Y	2024	Homing endonuclease I-Ppol-DNA complex:reaction at pH6.0 (K+ MES) with 500 uM Mn2+ for 600s	https://www.rcsb.org/structure/8VNO	RCSB Protein Data Bank, 8VNO
Chang C, Gao Y	2024	Homing endonuclease I-Ppol-DNA complex at pH6.0 (K+ MES) with 0.2 M sodium malonate	https://www.rcsb.org/structure/8VNP	RCSB Protein Data Bank, 8VNP
Chang C, Gao Y	2024	Homing endonuclease H98A I-Ppol-DNA complex at pH6.0 (K+ MES) with 1 mM Mn2+ for 1800s	https://www.rcsb.org/structure/8VNQ	RCSB Protein Data Bank, 8VNO

Continued on next page

Continued

Author(s)	Year	Dataset title	Dataset URL	Database and Identifier
Chang C, Gao Y	2024	Homing endonuclease H98A I-PpoI-DNA complex at pH6.0 (K+ MES) with 1 mM Mn ²⁺ for 600s and then 100 mM imidazole for 15 hrs	https://www.rcsb.org/structure/8VNR	RCSB Protein Data Bank, 8VNR
Chang C, Gao Y	2024	Homing endonuclease I-PpoI-DNA complex:reaction at pH6.0 (K+ MES) with 200 mM Mn ²⁺ for 600s	https://www.rcsb.org/structure/8VNS	RCSB Protein Data Bank, 8VNS
Chang C, Gao Y	2024	Homing endonuclease I-PpoI-DNA complex:reaction at pH6.0 (K+ MES) with 500 uM Mg ²⁺ for 1800s	https://www.rcsb.org/structure/8VNT	RCSB Protein Data Bank, 8VNT
Chang C, Gao Y	2024	Homing endonuclease H98A I-PpoI-DNA complex at pH6.0 (K+ MES) with 70 mM Tl ⁺ for 1800s	https://www.rcsb.org/structure/8VNU	RCSB Protein Data Bank, 8VNU

References

- Abelson J**, Trotta CR, Li H. 1998. tRNA splicing. *The Journal of Biological Chemistry* **273**:12685–12688. DOI: <https://doi.org/10.1074/jbc.273.21.12685>, PMID: 9582290
- Adams PD**, Afonine PV, Bunkóczi G, Chen VB, Davis IW, Echols N, Headd JJ, Hung L-W, Kapral GJ, Grosse-Kunstleve RW, McCoy AJ, Moriarty NW, Oeffner R, Read RJ, Richardson DC, Richardson JS, Terwilliger TC, Zwart PH. 2010. PHENIX: a comprehensive Python-based system for macromolecular structure solution. *Acta Crystallographica. Section D, Biological Crystallography* **66**:213–221. DOI: <https://doi.org/10.1107/S0907444909052925>, PMID: 20124702
- Adli M**. 2018. The CRISPR tool kit for genome editing and beyond. *Nature Communications* **9**:1911. DOI: <https://doi.org/10.1038/s41467-018-04252-2>, PMID: 29765029
- Arnould D**, Gaume B, Karbowski M, Sharpe JC, Cecconi F, Youle RJ. 2003. Mitochondrial release of AIF and EndoG requires caspase activation downstream of Bax/Bak-mediated permeabilization. *The EMBO Journal* **22**:4385–4399. DOI: <https://doi.org/10.1093/emboj/cdg423>, PMID: 12941691
- Ashworth J**, Havranek JJ, Duarte CM, Sussman D, Monnat RJ, Stoddard BL, Baker D. 2006. Computational redesign of endonuclease DNA binding and cleavage specificity. *Nature* **441**:656–659. DOI: <https://doi.org/10.1038/nature04818>, PMID: 16738662
- Auffinger P**, D'Ascenzo L, Ennifar E. 2016. *The alkali metal ions: their role for life*. Springer International Publishing. p. 167–201.
- Brändén G**, Neutze R. 2021. Advances and challenges in time-resolved macromolecular crystallography. *Science* **373**:eaba0954. DOI: <https://doi.org/10.1126/science.aba0954>, PMID: 34446579
- Carroll D**. 2014. Genome engineering with targetable nucleases. *Annual Review of Biochemistry* **83**:409–439. DOI: <https://doi.org/10.1146/annurev-biochem-060713-035418>, PMID: 24606144
- Chang C**, Lee Luo C, Gao Y. 2022. In crystallo observation of three metal ion promoted DNA polymerase misincorporation. *Nature Communications* **13**:2346. DOI: <https://doi.org/10.1038/s41467-022-30005-3>, PMID: 35487947
- Chen Y**, Gao T, Wang Y, Yang G. 2017. Investigating the influence of magnesium ions on p53–DNA binding using atomic force microscopy. *International Journal of Molecular Sciences* **18**:1585. DOI: <https://doi.org/10.3390/ijms18071585>
- Cheng YS**, Hsia KC, Doudeva LG, Chak KF, Yuan HS. 2002. The crystal structure of the nuclease domain of colicin E7 suggests a mechanism for binding to double-stranded DNA by the H-N-H endonucleases. *Journal of Molecular Biology* **324**:227–236. DOI: [https://doi.org/10.1016/s0022-2836\(02\)01092-6](https://doi.org/10.1016/s0022-2836(02)01092-6), PMID: 12441102
- Chevalier BS**, Stoddard BL. 2001. Homing endonucleases: structural and functional insight into the catalysts of intron/intein mobility. *Nucleic Acids Research* **29**:3757–3774. DOI: <https://doi.org/10.1093/nar/29.18.3757>, PMID: 11557808
- Chim N**, Meza RA, Trinh AM, Yang K, Chaput JC. 2021. Following replicative DNA synthesis by time-resolved X-ray crystallography. *Nature Communications* **12**:2641. DOI: <https://doi.org/10.1038/s41467-021-22937-z>, PMID: 33976175
- Christou N-E**, Apostolopoulou V, Melo DVM, Ruppert M, Fadini A, Henkel A, Sprenger J, Oberthuer D, Günther S, Pateras A, Rahmani Mashhour A, Yefanov OM, Galchenkova M, Reinke PYA, Kremling V, Scheer TES, Lange ER, Middendorf P, Schubert R, De Zitter E, et al. 2023. Time-resolved crystallography

- captures light-driven DNA repair. *Science* **382**:1015–1020. DOI: <https://doi.org/10.1126/science.adj4270>, PMID: 38033070
- Chu CY**, Rana TM. 2007. Small RNAs: regulators and guardians of the genome. *Journal of Cellular Physiology* **213**:412–419. DOI: <https://doi.org/10.1002/jcp.21230>, PMID: 17674365
- Cowan JA**. 2002. Structural and catalytic chemistry of magnesium-dependent enzymes. *Biometals* **15**:225–235. DOI: <https://doi.org/10.1023/a:1016022730880>, PMID: 12206389
- Das A**, Rai J, Roth MO, Shu Y, Medina ML, Barakat MR, Li H. 2023. Coupled catalytic states and the role of metal coordination in Cas9. *Nature Catalysis* **6**:969–977. DOI: <https://doi.org/10.1038/s41929-023-01031-1>, PMID: 38348449
- Deerfield DW**, Fox DJ, Head-Gordon M, Hiskey RG, Pedersen LG. 1991. Interaction of calcium and magnesium ions with malonate and the role of the waters of hydration: a quantum mechanical study. *Journal of the American Chemical Society* **113**:1892–1899. DOI: <https://doi.org/10.1021/ja00006a004>
- Demir M**, Russelburg LP, Lin W-J, Trasiña-Arenas CH, Huang B, Yuen PK, Horvath MP, David SS. 2023. Structural snapshots of base excision by the cancer-associated variant MutY N146S reveal a retaining mechanism. *Nucleic Acids Research* **51**:1034–1049. DOI: <https://doi.org/10.1093/nar/gkac1246>, PMID: 36631987
- Doudna JA**, Charpentier E. 2014. Genome editing. The new frontier of genome engineering with CRISPR-Cas9. *Science* **346**:1258096. DOI: <https://doi.org/10.1126/science.1258096>, PMID: 25430774
- Dupureur CM**. 2010. One is enough: insights into the two-metal ion nuclease mechanism from global analysis and computational studies. *Metallomics* **2**:609–620. DOI: <https://doi.org/10.1039/c0mt00013b>, PMID: 21072352
- Eastberg JH**, Eklund J, Monnat R, Stoddard BL. 2007. Mutability of an HNH nuclease imidazole general base and exchange of a deprotonation mechanism. *Biochemistry* **46**:7215–7225. DOI: <https://doi.org/10.1021/bi700418d>, PMID: 17516660
- Emsley P**, Lohkamp B, Scott WG, Cowtan K. 2010. Features and development of Coot. *Acta Crystallographica. Section D, Biological Crystallography* **66**:486–501. DOI: <https://doi.org/10.1107/S0907444910007493>, PMID: 20383002
- Flick KE**, Jurica MS, Monnat RJ, Stoddard BL. 1998. DNA binding and cleavage by the nuclear intron-encoded homing endonuclease I-PpoI. *Nature* **394**:96–101. DOI: <https://doi.org/10.1038/27952>, PMID: 9665136
- Freudenthal BD**, Beard WA, Shock DD, Wilson SH. 2013. Observing a DNA polymerase choose right from wrong. *Cell* **154**:157–168. DOI: <https://doi.org/10.1016/j.cell.2013.05.048>, PMID: 23827680
- Freudenthal BD**, Beard WA, Cuneo MJ, Dyrkheeva NS, Wilson SH. 2015. Capturing snapshots of APE1 processing DNA damage. *Nature Structural & Molecular Biology* **22**:924–931. DOI: <https://doi.org/10.1038/nsmb.3105>, PMID: 26458045
- Furuhata Y**, Kato Y. 2021. Asymmetric roles of two histidine residues in *Streptococcus pyogenes* Cas9 Catalytic domains upon chemical rescue. *Biochemistry* **60**:194–200. DOI: <https://doi.org/10.1021/acs.biochem.0c00766>, PMID: 33428390
- Galburt EA**, Chevalier B, Tang W, Jurica MS, Flick KE, Monnat RJ, Stoddard BL. 1999. A novel endonuclease mechanism directly visualized for I-PpoI. *Nature Structural Biology* **6**:1096–1099. DOI: <https://doi.org/10.1038/70027>, PMID: 10581547
- Galburt EA**, Chadsey MS, Jurica MS, Chevalier BS, Erho D, Tang W, Monnat RJ, Stoddard BL. 2000. Conformational changes and cleavage by the homing endonuclease I-PpoI: a critical role for A leucine residue in the active site. *Journal of Molecular Biology* **300**:877–887. DOI: <https://doi.org/10.1006/jmbi.2000.3874>, PMID: 10891275
- Gao Y**, Yang W. 2016. Capture of a third Mg²⁺ is essential for catalyzing DNA synthesis. *Science* **352**:1334–1337. DOI: <https://doi.org/10.1126/science.aad9633>, PMID: 27284197
- Garcin ED**, Hosfield DJ, Desai SA, Haas BJ, Björas M, Cunningham RP, Tainer JA. 2008. DNA apurinic-apyrimidinic site binding and excision by endonuclease IV. *Nature Structural & Molecular Biology* **15**:515–522. DOI: <https://doi.org/10.1038/nsmb.1414>, PMID: 18408731
- Gregory MT**, Gao Y, Cui Q, Yang W. 2021. Multiple deprotonation paths of the nucleophile 3'-OH in the DNA synthesis reaction. *PNAS* **118**:e2103990118. DOI: <https://doi.org/10.1073/pnas.2103990118>, PMID: 34088846
- Grindley NDF**, Whiteson KL, Rice PA. 2006. Mechanisms of site-specific recombination. *Annual Review of Biochemistry* **75**:567–605. DOI: <https://doi.org/10.1146/annurev.biochem.73.011303.073908>, PMID: 16756503
- Hsia K-C**, Chak K-F, Liang P-H, Cheng Y-S, Ku W-Y, Yuan HS. 2004. DNA binding and degradation by the HNH protein Cole7. *Structure* **12**:205–214. DOI: <https://doi.org/10.1016/j.str.2004.01.004>, PMID: 14962381
- James R**, Kleanthous C, Moore GR. 1996. The biology of E colicins: paradigms and paradoxes. *Microbiology* **142**:1569–1580. DOI: <https://doi.org/10.1099/13500872-142-7-1569>, PMID: 8757721
- Kabsch W**. 2010. XDS. *Acta Crystallographica. Section D, Biological Crystallography* **66**:125–132. DOI: <https://doi.org/10.1107/S0907444909047337>, PMID: 20124692
- Kao HI**, Bambara RA. 2003. The protein components and mechanism of eukaryotic Okazaki fragment maturation. *Critical Reviews in Biochemistry and Molecular Biology* **38**:433–452. DOI: <https://doi.org/10.1080/10409230390259382>, PMID: 14693726
- Khan FA**, Pandupuspitasari NS, Chun-Jie H, Ao Z, Jamal M, Zohaib A, Khan FA, Hakim MR, ShuJun Z. 2016. CRISPR/Cas9 therapeutics: a cure for cancer and other genetic diseases. *Oncotarget* **7**:52541–52552. DOI: <https://doi.org/10.18632/oncotarget.9646>, PMID: 27250031
- Kiser PD**, Lorimer GH, Palczewski K. 2009. Use of thallium to identify monovalent cation binding sites in GroEL. *Acta Crystallographica. Section F, Structural Biology and Crystallography Communications* **65**:967–971. DOI: <https://doi.org/10.1107/S1744309109032928>, PMID: 19851000

- Li C-L, Hor L-I, Chang Z-F, Tsai L-C, Yang W-Z, Yuan HS. 2003. DNA binding and cleavage by the periplasmic nuclease Vvn: a novel structure with a known active site. *The EMBO Journal* **22**:4014–4025. DOI: <https://doi.org/10.1093/emboj/cdg377>, PMID: 12881435
- Lin JLJ, Nakagawa A, Skeen-Gaar R, Yang W-Z, Zhao P, Zhang Z, Ge X, Mitani S, Xue D, Yuan HS. 2016. Oxidative stress impairs cell death by repressing the nuclease activity of mitochondrial endonuclease G. *Cell Reports* **16**:279–287. DOI: <https://doi.org/10.1016/j.celrep.2016.05.090>, PMID: 27346342
- Maestre-Reyna M, Wang P-H, Nango E, Hosokawa Y, Saft M, Furrer A, Yang C-H, Gusti Ngurah Putu EP, Wu W-J, Emmerich H-J, Caramello N, Franz-Badur S, Yang C, Engilberge S, Wranik M, Glover HL, Weinert T, Wu H-Y, Lee C-C, Huang W-C, et al. 2023. Visualizing the DNA repair process by a photolyase at atomic resolution. *Science* **382**:eadd7795. DOI: <https://doi.org/10.1126/science.add7795>, PMID: 38033054
- Maghsoud Y, Jayasinghe-Arachchige VM, Kumari P, Cisneros GA, Liu J. 2023. Leveraging QM/MM and molecular dynamics simulations to decipher the reaction mechanism of the Cas9 HNH domain to investigate off-target effects. *Journal of Chemical Information and Modeling* **63**:6834–6850. DOI: <https://doi.org/10.1021/acs.jcim.3c01284>, PMID: 37877218
- Marti TM, Fleck O. 2004. DNA repair nucleases. *Cellular and Molecular Life Sciences* **61**:336–354. DOI: <https://doi.org/10.1007/s00018-003-3223-4>, PMID: 14770297
- Mimitou EP, Symington LS. 2009. DNA end resection: many nucleases make light work. *DNA Repair* **8**:983–995. DOI: <https://doi.org/10.1016/j.dnarep.2009.04.017>, PMID: 19473888
- Moon AF, Midon M, Meiss G, Pingoud A, London RE, Pedersen LC. 2011. Structural insights into catalytic and substrate binding mechanisms of the strategic EndA nuclease from *Streptococcus pneumoniae*. *Nucleic Acids Research* **39**:2943–2953. DOI: <https://doi.org/10.1093/nar/gkq1152>, PMID: 21113026
- Moore MJ, Proudfoot NJ. 2009. Pre-mRNA processing reaches back to transcription and ahead to translation. *Cell* **136**:688–700. DOI: <https://doi.org/10.1016/j.cell.2009.02.001>, PMID: 19239889
- Morin A, Eisenbraun B, Key J, Sanschagrin PC, Timony MA, Ottaviano M, Sliz P. 2013. Collaboration gets the most out of software. *eLife* **2**:e01456. DOI: <https://doi.org/10.7554/eLife.01456>, PMID: 24040512
- Nakamura T, Zhao Y, Yamagata Y, Hua Y, Yang W. 2012. Watching DNA polymerase η make a phosphodiester bond. *Nature* **487**:196–201. DOI: <https://doi.org/10.1038/nature11181>, PMID: 22785315
- Nakamura T, Yamagata Y. 2022. Visualization of mutagenic nucleotide processing by. *PNAS* **119**:2203118119. DOI: <https://doi.org/10.1073/pnas.2203118119>
- Nierzwicki Ł, East KW, Binz JM, Hsu RV, Ahsan M, Arantes PR, Skeens E, Pacesa M, Jinek M, Lisi GP, Palermo G. 2022. Principles of target DNA cleavage and the role of Mg²⁺ in the catalysis of CRISPR-Cas9. *Nature Catalysis* **5**:912–922. DOI: <https://doi.org/10.1038/s41929-022-00848-6>, PMID: 36778082
- Patel AA, Steitz JA. 2003. Splicing double: insights from the second spliceosome. *Nature Reviews. Molecular Cell Biology* **4**:960–970. DOI: <https://doi.org/10.1038/nrm1259>, PMID: 14685174
- Pommer AJ, Cal S, Keeble AH, Walker D, Evans SJ, Kühlmann UC, Cooper A, Connolly BA, Hemmings AM, Moore GR, James R, Kleantous C. 2001. Mechanism and cleavage specificity of the H-N-H endonuclease colicin E9. *Journal of Molecular Biology* **314**:735–749. DOI: <https://doi.org/10.1006/jmbi.2001.5189>, PMID: 11733993
- Ran FA, Hsu PD, Wright J, Agarwala V, Scott DA, Zhang F. 2013. Genome engineering using the CRISPR-Cas9 system. *Nature Protocols* **8**:2281–2308. DOI: <https://doi.org/10.1038/nprot.2013.143>, PMID: 24157548
- Reed AJ, Suo Z. 2017. Time-dependent extension from an 8-oxoguanine lesion by human DNA polymerase beta. *Journal of the American Chemical Society* **139**:9684–9690. DOI: <https://doi.org/10.1021/jacs.7b05048>, PMID: 28682600
- Samara NL, Yang W. 2018. Cation trafficking propels RNA hydrolysis. *Nature Structural & Molecular Biology* **25**:715–721. DOI: <https://doi.org/10.1038/s41594-018-0099-4>, PMID: 30076410
- Schwank G, Koo B-K, Sasselli V, Dekkers JF, Heo I, Demircan T, Sasaki N, Boymans S, Cuppen E, van der Ent CK, Nieuwenhuis EES, Beekman JM, Clevers H. 2013. Functional repair of CFTR by CRISPR/Cas9 in intestinal stem cell organoids of cystic fibrosis patients. *Cell Stem Cell* **13**:653–658. DOI: <https://doi.org/10.1016/j.stem.2013.11.002>, PMID: 24315439
- Sharma G, Sharma AR, Bhattacharya M, Lee SS, Chakraborty C. 2021. CRISPR-Cas9: a preclinical and clinical perspective for the treatment of human diseases. *Molecular Therapy* **29**:571–586. DOI: <https://doi.org/10.1016/j.ymthe.2020.09.028>, PMID: 33238136
- Shen BW, Landthaler M, Shub DA, Stoddard BL. 2004. DNA binding and cleavage by the HNH homing endonuclease I-Hmul. *Journal of Molecular Biology* **342**:43–56. DOI: <https://doi.org/10.1016/j.jmb.2004.07.032>, PMID: 15313606
- Shen B, Singh P, Liu R, Qiu J, Zheng L, Finger LD, Alas S. 2005. Multiple but dissectible functions of FEN-1 nucleases in nucleic acid processing, genome stability and diseases. *BioEssays* **27**:717–729. DOI: <https://doi.org/10.1002/bies.20255>, PMID: 15954100
- Sorek R, Kunin V, Hugenholtz P. 2008. CRISPR—a widespread system that provides acquired resistance against phages in bacteria and archaea. *Nature Reviews. Microbiology* **6**:181–186. DOI: <https://doi.org/10.1038/nrmicro1793>, PMID: 18157154
- Stoddard BL. 2005. Homing endonuclease structure and function. *Quarterly Reviews of Biophysics* **38**:49–95. DOI: <https://doi.org/10.1017/S0033583505004063>, PMID: 16336743
- Sun W, Yang J, Cheng Z, Amrani N, Liu C, Wang K, Ibrahim R, Edraki A, Huang X, Wang M, Wang J, Liu L, Sheng G, Yang Y, Lou J, Sontheimer EJ, Wang Y. 2019. Structures of *Neisseria meningitidis* Cas9 complexes in catalytically poised and anti-CRISPR-inhibited states. *Molecular Cell* **76**:938–952. DOI: <https://doi.org/10.1016/j.molcel.2019.09.025>, PMID: 31668930

- Tock MR**, Dryden DTF. 2005. The biology of restriction and anti-restriction. *Current Opinion in Microbiology* **8**:466–472. DOI: <https://doi.org/10.1016/j.mib.2005.06.003>, PMID: 15979932
- Tsutakawa SE**, Shin DS, Mol CD, Izumi T, Arvai AS, Mantha AK, Szczesny B, Ivanov IN, Hosfield DJ, Maiti B, Pique ME, Frankel KA, Hitomi K, Cunningham RP, Mitra S, Tainer JA. 2013. Conserved structural chemistry for incision activity in structurally non-homologous apurinic/aprimidinic endonuclease APE1 and endonuclease IV DNA repair enzymes. *The Journal of Biological Chemistry* **288**:8445–8455. DOI: <https://doi.org/10.1074/jbc.M112.422774>, PMID: 23355472
- Vyas R**, Reed AJ, Tokarsky EJ, Suo Z. 2015. Viewing human DNA polymerase β faithfully and unfaithfully bypass an oxidative lesion by time-dependent crystallography. *Journal of the American Chemical Society* **137**:5225–5230. DOI: <https://doi.org/10.1021/jacs.5b02109>, PMID: 25825995
- Whitaker AM**, Flynn TS, Freudenthal BD. 2018. Molecular snapshots of APE1 proofreading mismatches and removing DNA damage. *Nature Communications* **9**:399. DOI: <https://doi.org/10.1038/s41467-017-02175-y>, PMID: 29374164
- Wilson MA**. 2022. Mapping enzyme landscapes by time-resolved crystallography with synchrotron and X-Ray free electron laser light. *Annual Review of Biophysics* **51**:79–98. DOI: <https://doi.org/10.1146/annurev-biophys-100421-110959>, PMID: 34932909
- Wu J**, Samara NL, Kuraoka I, Yang W. 2019. Evolution of inosine-specific endonuclease V from bacterial DNase to Eukaryotic RNase. *Molecular Cell* **76**:44–56. DOI: <https://doi.org/10.1016/j.molcel.2019.06.046>, PMID: 31444105
- Wu CC**, Lin JLJ, Yuan HSS. 2020. Structures, mechanisms, and functions of his-me finger nucleases. *Trends in Biochemical Sciences* **45**:935–946. DOI: <https://doi.org/10.1016/j.tibs.2020.07.002>, PMID: 32807610
- Yang W**. 2008. An equivalent metal ion in one- and two-metal-ion catalysis. *Nature Structural & Molecular Biology* **15**:1228–1231. DOI: <https://doi.org/10.1038/nsmb.1502>, PMID: 18953336
- Yang W**. 2011. Nucleases: diversity of structure, function and mechanism. *Quarterly Reviews of Biophysics* **44**:1–93. DOI: <https://doi.org/10.1017/S0033583510000181>, PMID: 20854710
- Zhang Y**, Zhang H, Xu X, Wang Y, Chen W, Wang Y, Wu Z, Tang N, Wang Y, Zhao S, Gan J, Ji Q. 2020. Catalytic-state structure and engineering of *Streptococcus thermophilus* Cas9. *Nature Catalysis* **3**:813–823. DOI: <https://doi.org/10.1038/s41929-020-00506-9>
- Zhu X**, Clarke R, Puppala AK, Chittori S, Merk A, Merrill BJ, Simonović M, Subramaniam S. 2019. Cryo-EM structures reveal coordinated domain motions that govern DNA cleavage by Cas9. *Nature Structural & Molecular Biology* **26**:679–685. DOI: <https://doi.org/10.1038/s41594-019-0258-2>, PMID: 31285607